Methodology for Reduced-Order Multichannel Modeling of a Catalytic Converter

(article starts on next page)

Article

Methodology for Reduced-Order Multichannel Modeling of a Catalytic Converter

Pratheeba Chanda Nagarajan, Henrik Ström,* and Jonas Sjöblom*

Read Online

ACCESS | Metrics & More | Article Recommendations | Supporting Information

ABSTRACT: Numerical simulations of catalytic exhaust after treatment systems are critical for evaluation and optimization. While transient 3D-computational fluid dynamics (3D-CFD) simulations are computationally expensive, single channel models (SCM) are robust and computationally effective, but flow maldistribution that compromises the accuracy of SCM is unavoidable in realistic geometries. We present a novel multi-channel model (MCM) by applying chemometric techniques on transient 3D-CFD solutions. The performance of an oxidation catalyst with flow maldistribution is simulated and variables of interest are collected at the catalyst outlet for calibration and assessment of the MCM. Channel locations and weights are determined using D-optimal design on the scores from a principal component analysis, followed by weighted least-squares regression based on two objective functions (heat content and species conversion). MCM exhibits lower residuals than a SCM and closely approximates the computational fluid dynamics data across various test cases, opening up for rigorous control applications with improved accuracy in real-world systems with intricate geometries.
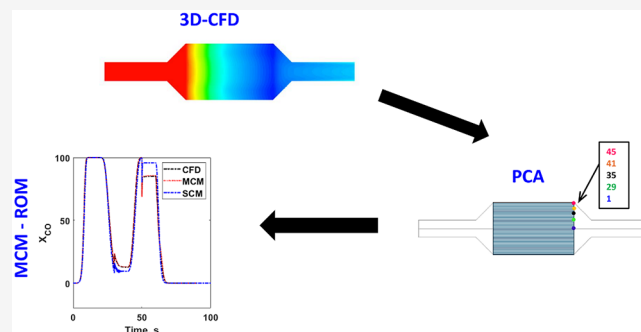
INTRODUCTION

The use of hydrocarbon-based fuels in automobiles and power plants results in emissions, such as carbon monoxide, particulate matter, nitrogen oxides, and hydrocarbons that adversely affect human health and the environment.[1] Emission legislations are in place for more than three decades and are constantly made more stringent, to reduce the negative consequences of pollution.[2] To comply with the regulations on the emission of carbon monoxide (CO), nitrogen oxide, and hydrocarbon (HC), it is crucial to use catalytic converters to treat the exhaust from automotive engines. These converters are an integral part of emissions control and are popular due to their high efficiency and selectivity. The catalytic converters require constant improvement in their performance to meet ever-increasing limits on exhaust emissions.

Multiple catalytic converters form the exhaust after treatment system (EATS) train for emissions control. Several processes like transport of mass, momentum, and energy in addition to surface reactions, adsorption, and desorption of the species occur in catalytic converters, making their operation complex with large span of time scales and length scales. Scientific advances in these devices that were primarily empirical are becoming increasingly dependent on computer simulations and improved mathematical modeling. Catalytic converters, often designated as honeycomb monoliths, are multichannel cylindrical structures in a metal casing.[3] One goal of a mathematical model for a catalytic converter is to precisely represent all the physics and chemistry that take place at every

level, for example, the transport processes in the catalytic converters on a macroscopic scale versus detailed kinetic mechanisms for the catalytic reactions that occur on the surface and the tortuous path taken by the species in the washcoat and pores, at the microscopic scale.[4−6] However, the computational demands of an all-encompassing kind of simulation imply that these approaches cannot be used for real-time applications and remain too ineffective for design or optimization studies, where a large number of simulation runs are needed.

Flow distribution assumptions and heat and mass interactions in these devices form the basis of the classification of modeling. Lower dimensional models, such as 1D models and higher-dimensional models, are adopted to obtain the solution for these models, having their respective assumptions.

First, we consider the single channel model (SCM). Here, the flow is implicitly assumed to be uniformly distributed among all channels and there is no channel-to-channel exchange of heat, mass, or momentum. In the absence of flow maldistribution and under adiabatic conditions, every

channel will indeed behave similarly to all other channels in terms of reactive transport processes. This implies that every channel experiences the same volumetric flow rate, temperature, and species concentrations at its inlet. This channel is thought to be the representative channel, and it is sufficient to model this representative channel to capture the performance of the entire monolith. Energy and species transport are modeled as partial differential equations (PDEs) with the velocity specified. Reactions can occur in the gas phase and on the wall in the solid phase. Species balance equations and energy balance equations for these two phases are connected to each other through transport equations. The species concentrations and temperature on the wall can be resolved to get a heterogeneous model that includes resistances as film coefficients, eliminating the need for an effectiveness factor for apparent rates with the gas phase concentration.[7] If mixed-cup concentrations and temperatures are used both in the fluid and solid phases, disregarding the internal and external mass-transfer resistances, a pseudohomogeneous model can be obtained.[7] These modeling challenges are all present, irrespective of the rate expressions that are employed. In fact, the computational demands for 3D models can be significant even for basic kinetic models.[8]

Considering the complex dynamics of catalytic converters, particularly in terms of flow distribution and reactive transport processes, various mathematical models have been devised to simulate their performance. 1D models solve for the species concentration and temperature,[9,10] accounting for simultaneous mass transfer, chemical reaction, and heat transfer,[11] incorporating detailed kinetics[12,13] and washcoat diffusion,[14] internal mass-transfer resistances by using an effectiveness factor[15−18] and 1 + 1D models.[19−21]

In real applications, the space requirements and placement of catalytic converters in the exhaust line give rise to flow maldistribution and varying heat- and mass-transfer rates across the catalyst channels. These effects, along with the interchannel dynamics (mediated primarily via heat conduction), result in flow differences at the inlet of the monolith, demanding higher dimensional models with heat interactions. One way to account for these effects is by implementing a system-wide model,[22] where a series of aftertreatment devices are modeled with detailed species and thermal balances. Alternatively, a more descriptive approach of computational fluid dynamics (CFD) methods such as large eddy simulations can be performed.[23]

An appropriate way to capture the intricate interactions between chemical reactions and momentum, heat, and mass transport is to use CFD modeling. The CFD approach completely alleviates the need to make any a priori assumptions on the flow uniformity and result in a closer agreement with experimental data.[24,25]

Some works have attempted to model all channels of the monolith for EATS,[26−28] sometimes symmetry about a plane is assumed to reduce the computational costs. More often, the computational load is reduced by invoking the porous media assumption in EATS modeling,[29] in which the gradients in the continuum fields are not resolved on the individual catalyst channels level but represented by their cross-sectional averages. Hayes et al. conducted computational simulations on a catalytic converter, with simulation times ranging from under a minute for steady-state cold flow tests to 2 h for transient light-off simulations.[30]

CFD studies were employed for pulsating inlet conditions of EATS with porous media assumption.[31,32] Reactive simulations[33] and nonreactive simulations[34] were developed to study the effect of flow maldistribution in terms of uniformity indices, where the flow field was solved using Reynolds averaged Navier−Stokes (RANS) equations. Further, CFD simulations were performed to assess flow maldistribution under cold start conditions.[35] With complex geometries involving bends, 3D simulations are important to capture performance characteristics.[36]

The SCM models[9−21] are popular because of their lower computational costs. However, when flow maldistribution is an issue, CFD studies[24,25,36,37] are required for accuracy. In the context of EATS modeling with flow maldistribution, we have shown in our earlier works[34] that under transient conditions, the flow and temperature fields exhibit a considerable spatiotemporal variation. This would also imply that specifying a single velocity and temperature at the inlet for all of the channels would produce inaccurate results.

The complexity of catalytic converters in terms of time-scale span, strong velocity−temperature interaction, and nonlinearity of chemical kinetics can be well characterized in CFD simulations. The computational cost of such simulations, however, renders them unfit for real-time evaluation, optimization, or iterative design. The computational load can be reduced by using several 1D models in parallel.[38] Such multichannel models (MCMs) of catalytic converters have several advantages over single-channel models or full 3D-CFD models. They can provide a more accurate representation of the actual flow field in the converter, which can lead to better predictions of the conversion efficiency and temperature distribution. They can be used for optimal design and operation of the EATS,[4] such as in determining the catalyst size, layout, loading, grading, and/or dosing strategy in selective catalytic reduction (SCR)[39] to reduce ammonia slip in the exhausts. Further, under stringent emission legislations, such as Euro VI, EATS models are also used for onboard control and dosing purposes; here control algorithms require models with better accuracy.

Consequently, our goal is to construct these reduced-order MCMs by applying the multivariate data analysis (MVDA) procedure on the set of CFD results. Capturing the distribution of the flow field in terms of variances and applying a model reduction procedure can form the basis for this MCM. Such a procedure could offer advantages in predicting the performance under difficult conditions, such as cold start and real driving emissions, in addition to generic driving conditions in comparison to conventional approaches disregarding the influence of flow maldistribution. In this work, we present the methodology of developing a MCM from a full 3D-CFD solution set, by applying chemometric techniques like principal component analysis (PCA), D-optimal design, and multiple linear regression. Additionally, we characterize and quantify the MCM performance compared to a conventional SCM and the full CFD by using reactive simulations in a diesel oxidation catalyst (DOC).

It should be noted that the proposed MCM concept differs from superficially similar works in the literature. Most notably, Chakravarthy et al.[35] devised a MCM in which intrinsic monolith channels were arbitrarily lumped into fewer representative channels by employing a coarser computational mesh in the CFD simulations, and Aslanjan et al.[38] developed a MCM where the monolith is divided into a user-specified

number of representative SCMs that receive spatiotemporally varying inlet boundary conditions prescribed from experimental data and with tunable radial heat conduction between channels. These approaches do resolve variations inside the monolith but do not offer a methodology for determining the number of representative channels to employ or their positions. Furthermore, although less expensive than full 3D-CFD, these approaches do not offer a way to develop standalone MCMs of CFD-like accuracy at computational performance relevant for online monitoring and onboard diagnostics.

MVDA procedures have previously been applied to computationally intensive processes like combustion kinetics.[40,41] However, this work presents the first application of chemometric techniques to derive a MCM from first-principles CFD output of an exhaust aftertreatment component. In this work, transient reactive CFD simulations form the basis on which MVDA techniques are applied. A DOC with global kinetics based on the work of Pandya et al.[42] is chosen. PCA is a dimensionality reduction technique,[43] which can be applied on a large data set like transient reactive CFD solution. Here, a smaller number of components, called the principal components, is sufficient to explain the variance in the original data. The D-optimal design procedure can then be applied on the scores matrix to further precisely identify the information presented from principal components.[44] Weighted least-squares (WLS) can be used to quantify the performance of the reduced order model by defining appropriate objective functions. First, a PCA is applied on the transient CFD output to identify the number of channels required to describe the real catalyst behavior with accuracy close to that of the full CFD. Following the PCA, a D-optimal design procedure is used to identify the actual channel identity. The WLS method is subsequently applied to derive the weights needed to obtain the mixed-cup prediction from the MCM. The mixed-cup quantities refer to the mass weighted average values of the solution variables, as defined in ANSYS Fluent.

The paper is organized as follows: we start first with the modeling methodology presenting the CFD model and the 1D-SCM equations (formulated as a tanks-in-series model) in the Modeling Section, covering the description of geometry, boundary conditions, and initial conditions. Numerical simulations and the model order reduction procedure and results are presented and discussed in the Results and Discussion Section. In the Computational Efficiency Section, conclusions are drawn, and future directions are presented. The Supporting Information provides details of modeling and the theoretical background of the various MVDA methods used in this work.

MODELING

This section presents the details of the methodology of modeling. The aim of the work is to present a reduced-order model that has the accuracy of a 3D-CFD model but at a computational cost lower than that of a 1D-SCM model. Therefore, we present the model formulation of both 3D-CFD and 1D-SCM models, followed by the PCA and D-optimal design procedure to derive the MCM.

Geometry. We choose to work with an after treatment device to illustrate the methodology of obtaining reduced order models. The catalyst measures 25.4 mm in diameter, 76.2 mm in length, and 400 cpsi. This choice of size is akin to that of Pandya et al.[42] In our configuration, however, we have

added equal-sized front and rear cones to the catalyst, each inclined at 45°, connected by 8.5 mm diameter pipes serving as inlet and outlet sections. The resulting system spans a length of 218 mm, as depicted in Figure 1. The spatial resolution is in the range of 0.06−0.6 mm at mesh-independent conditions.
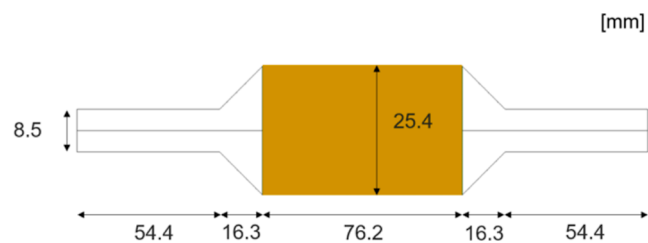

Figure 1. Schematic of the geometry used in the present work. The flow is from left to right. The shaded yellow section represents the catalytic region.

The catalytic section is modeled as a porous medium. The porous medium has a porosity of 0.69, corresponding to the open frontal area of the catalyst brick. As the flow in the catalyst channels is laminar, the source term of the momentum balance equation is modeled as a pure viscous resistance term

$$S_i = -\frac{\mu}{\alpha}u_i \tag{1}$$

where α is the permeability (taken as 2.111×10^{-8} m^2 to match the pressure drop over the catalyst) in the mean flow direction and three orders of lower magnitude in the other coordinate directions (taken as 2.111×10^{-11} m^2). The thermal equilibrium is also assumed between the catalyst solid and the gas with an effective volume-weighted heat conduction. This assumption holds as the Sparrow number, a dimensionless number, which is ratio of the equilibrium conduction thermal resistance to the convection thermal resistance for the entire porous domain, is large ($O10^2$).[45]

Kinetics. Chemical reactions corresponding to those in a conventional DOC occur in the catalyst and produce the source terms for the energy balance and species mass balance in the catalyst region. The relevant reactions include: oxidation of CO, H$_2$, and HC, and reversible oxidation of NO to NO$_2$. Further, NO is also reduced by HC at low temperatures. These reactions are represented by global kinetic rate expressions in the reaction mechanism adopted from Pandya et al.[42] and provided in Table 1. In this mechanism, HC is represented by C$_3$H$_6$.

As seen in Table 1, the catalytic rate expressions (kmol/m$_{cat}^2$ s) are based on the catalyst surface area. These rates are based on global kinetics and are apparent reaction rates, assuming unity effectiveness factor. Further, honeycomb monolith reactors have typically a large surface area per unit volume and smaller transfer resistances, the Thiele modulus of these reactors are very small, with unity effectiveness factor, implying larger part of the catalyst surface can be effectively utilized for reactions.[46] To ensure dimensional homogeneity in the kinetic source term in the species balance equation, a multiplication factor (product of surface area per volume of catalyst and molecular weight of the species) is used and corrected for the volume fraction of the solid with porosity of the catalytic converter in the reaction mechanism adopted from Pandya et al.[42] The heats of reactions are carefully calculated from heat capacity quartic polynomial expressions for all species, that are

Table 1. DOC Kinetics and Global Rate Expressions by Pandya et al.[42][a]

reaction	global rate expression ($kmol/m_{cat}^2\ s$)
R1: $CO + \frac{1}{2}O_2 \rightarrow CO_2$	$\dfrac{k_1 X_{CO} X_{O_2}}{G}$
R2: $C_3H_6 + \frac{7}{2}O_2 + 2NO \rightarrow 3CO_2 + 3H_2O + N_2$	$\dfrac{k_2 X_{C_3H_6} X_{NO} X_{O_2}}{G G_4}$
R3: $C_3H_6 + \frac{9}{2}O_2 \rightarrow 3CO_2 + 3H_2O$	$\dfrac{k_2 X_{C_3H_6} X_{O_2}}{G}$
R4: $NO + \frac{1}{2}O_2 \leftrightarrow NO_2$	$\dfrac{k_3(X_{NO} X_{O_2}^{0.5} - P^{-0.5} X_{NO_2}/K_{EQ})}{G}$
R5: $H_2 + \frac{1}{2}O_2 \rightarrow H_2O$	$\dfrac{k_1 X_{H_2} X_{O_2}}{G}$

Adsorption Inhibition Factors

$G = T G_1 G_2 G_3$
$G_1 = (1 + K_1 X_{CO} + K_2 X_{C3H6})^2$
$G_2 = 1 + K_3 (X_{CO} X_{C3H6})^2$
$G_3 = 1 + K_4 X_{NO}$
$G_4 = 1 + K_5 X_{O2}$

Kinetic Constants

$k_1 = 1.93 \times 10^{11} \exp\left(\dfrac{-51873}{R}\left[\dfrac{1}{T} - \dfrac{1}{450}\right]\right)$

$k_2 = 1 \times 10^9 \exp\left(\dfrac{-90000}{R}\left[\dfrac{1}{T} - \dfrac{1}{450}\right]\right)$

$k_3 = 2.83 \times 10^7 \exp\left(\dfrac{-21341}{R}\left[\dfrac{1}{T} - \dfrac{1}{450}\right]\right)$

$K_1 = 648.6 \exp\left(\dfrac{6574}{R}\left[\dfrac{1}{T} - \dfrac{1}{450}\right]\right)$

$K_2 = 2.21 \times 10^4 \exp\left(\dfrac{13226}{R}\left[\dfrac{1}{T} - \dfrac{1}{450}\right]\right)$

$K_3 = 5.792 \times 10^{13} \exp\left(\dfrac{40000}{R}\left[\dfrac{1}{T} - \dfrac{1}{450}\right]\right)$

$K_4 = 3.63 \times 10^4 \exp\left(\dfrac{4482}{R}\left[\dfrac{1}{T} - \dfrac{1}{450}\right]\right)$

$K_5 = 3.679 \exp\left(\dfrac{-67207}{R}\left[\dfrac{1}{T} - \dfrac{1}{450}\right]\right)$

$\ln(K_{EQ}) = 5.0462 + \dfrac{6343.4}{T} - 2.2973 \ln(T) + 3.0315 \times 10^{-3} T$
$- 8.2812 \times 10^{-7} T^2 + 1.1412 \times 10^{-10} T^3$

[a]X_i represents the mole fraction of species i, k_j are rate coefficients, K_j are adsorption equilibrium constants, and G_j are inhibition terms. R is the universal gas constant, T is the temperature (K).

functions of temperature.[47] Enthalpy and heats of reactions are calculated as functions of composition and temperature following the procedure shown in thermodynamic texts[47] to account for changes in temperature from the standard states.[47]

Figure 2 is a summary of the model development procedure for obtaining reduced order models combining CFD solutions and MVDA techniques.

3D-CFD Model. Unsteady state RANS equations are used to model the equations of continuity, momentum, energy, and species conservation. SST-κ—ω model is used to model turbulence. The catalytic section is approximated using a porous media approximation. The details are provided in the Supporting Information.

1D-SCM Model. A monolithic reactor has a large number of channels that all have the same size and shape. The basic assumption in the SCM is that all channels are identical and subject to the same inlet conditions. There is no transport of mass between the channels. In reality, the walls permit heat conduction, axially and radially, which introduces heat exchange between channels. In a conventional SCM model, however, this is neglected, and the channel is assumed to be adiabatic. The flow in the monolith is essentially laminar. The contribution of radiative heat transfer is neglected here. The monolith is described by a pseudohomogeneous model for the reactions, which implies that the bulk species concentration is the same as the surface concentration. This approach is also in accordance with the porous media assumption employed in the CFD model. Also, the solid temperature is assumed to be equal to the gas phase temperature, in analogy with the thermal equilibrium assumption in the CFD. With these assumptions,
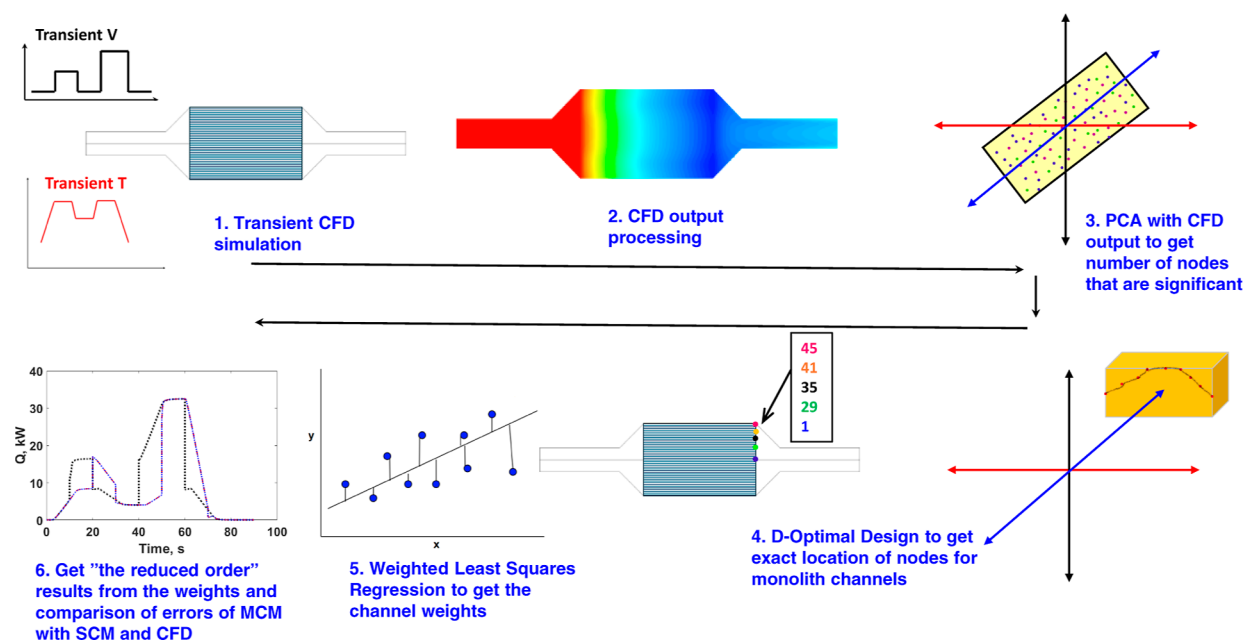
Figure 2. Schematic representation of the reduced order model development process.

Table 2. Transient Inlet Profiles for Calibration and Test Cases

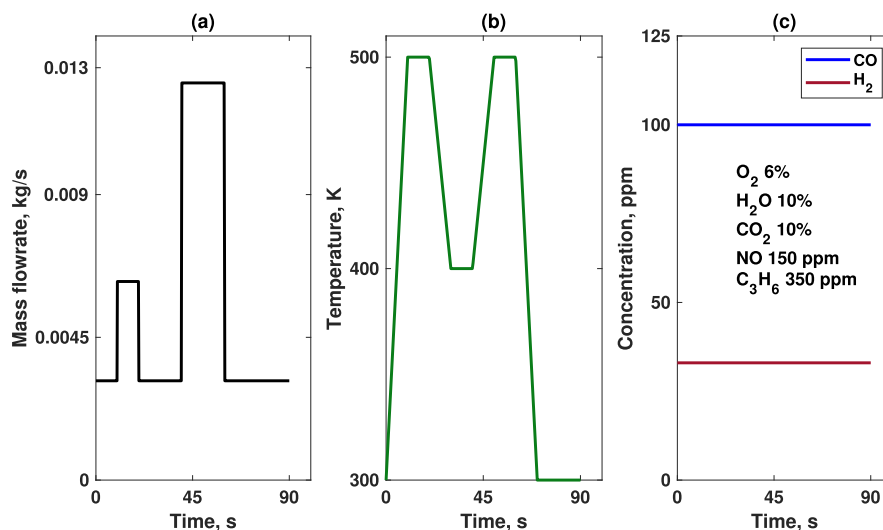|	profile			
case number	mass flow rate	temperature	concentration	figure labels
calibration case	V_1	T_1	constant	Figure 3
test case 1	V_1	T_1	variable	Figure 4
test case 2	V_2	T_1	constant	Figure 5
test case 3	V_2	T_1	variable	Figure 6

Figure 3. Profiles of (a) mass flow rate, (b) temperature, and (c) concentrations for the calibration case.

the governing mass balance for the transient 1D-SCM take the form of PDEs, with solution sought for concentrations of species and temperature.[48]

Numerically, these equations are solved using the tanks-in-series approach, wherein the PDEs are converted into a system of ordinary differential equations (ODEs).[49] The number of tanks in series is chosen to be identical to the number of cells across the catalyst brick in the CFD simulation so that the

numerical dispersion along the channel axis is identical in both the 3D-CFD and the 1D-SCM approaches.

Boundary and Initial Conditions. The CFD simulations were performed by using ANSYS Fluent 2022 R2. The simulations were run for a duration of approximately 90 s, during which the prescribed inlet conditions (velocity, temperature, and species concentrations) were dynamically adjusted according to the temporal profiles provided in Table 2. Transient test cases, which are segments of standardized test
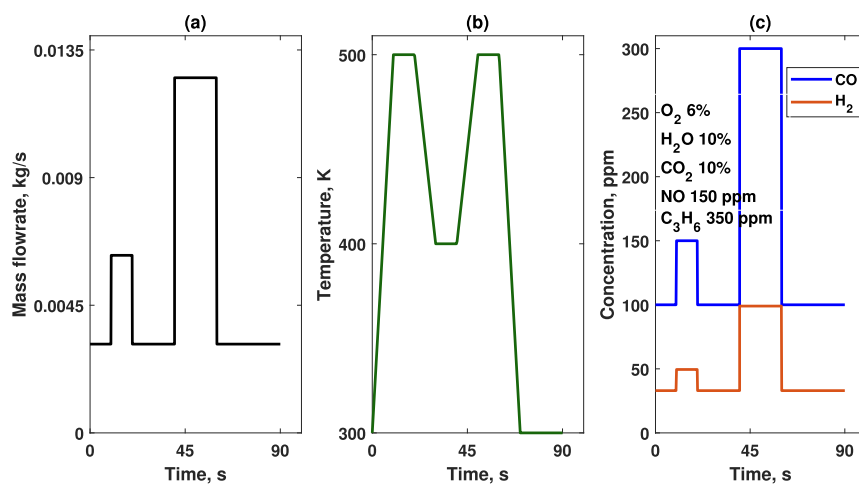
Figure 4. Profiles of (a) mass flow rate, (b) temperature, and (c) concentrations for test case 1. Here, the CO and H_2 concentrations vary with time.

Figure 5. Profiles of (a) mass flow rate, (b) temperature, and (c) concentrations for test case 2. Here, the mass flow rate is shifted by 10 s as compared to the calibration case.
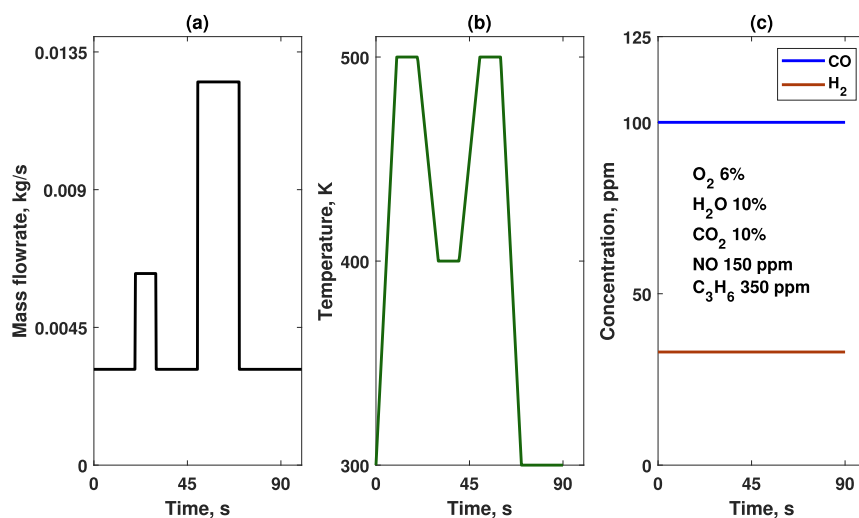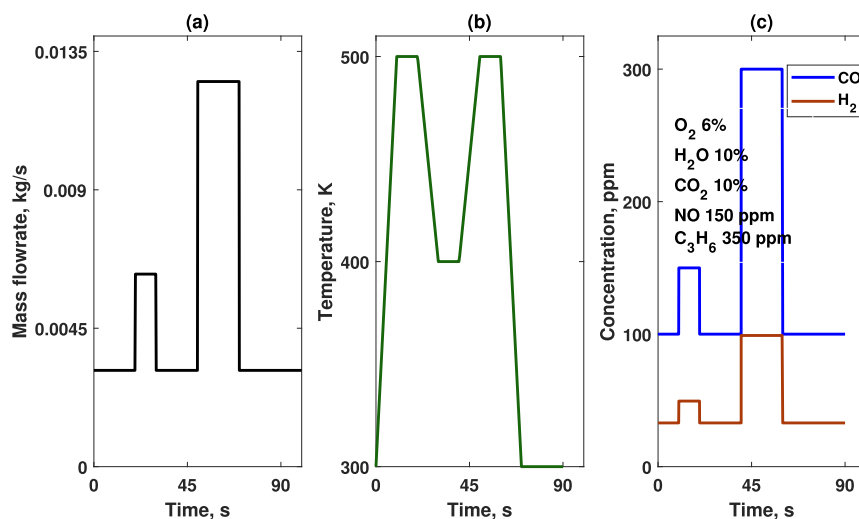

Figure 6. Profiles of (a) mass flow rate, (b) temperature, and (c) concentration for test case 3. Here, the mass flow rate is shifted by 10 s as compared to the calibration case, and the CO and H_2 concentrations also vary with time.
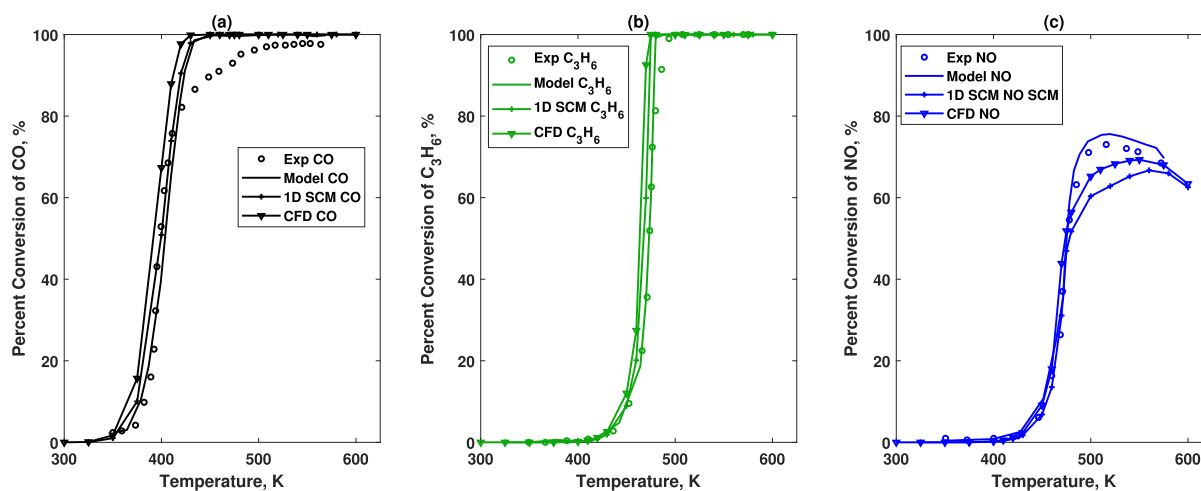
Figure 7. Profiles of steady-state conversion of species as a function of temperature: comparison of experiments in Pandya et al.[42] with the current 3D-CFD and 1D-SCM. Here, the panels are for the species CO, C_3H_6, and NO, respectively. Experimental data ("Exp") and simulations from Pandya et al.[42] ("Model") are shown with open circles and lines without markers, whereas our simulations (1D-SCM and 3D-CFD) are shown as lines with filled circles and triangles, respectively.

cycles, are chosen to model the dynamic behavior, such as catalyst heating, valve operations, and degree of complete combustion.

The mass flow rate transients feature rectangular pulses at three levels (31.3, 62.6, and 125 g/s). The temperature transients have the minimum and maximum at 300 and 500 K, respectively, passing through the intermediate level of 450 K. These temperatures cover before and after the reactant species' light-off temperatures and the cold-start temperature of the catalyst. Concentration values of species are adopted from Pandya et al.,[42] and additionally a variable concentration case is devised (cf. Figures 4 and 6). A total of three test cases (cf. Figures 4−6) and a calibration case form the test matrix for the reactive simulations.

Standard wall functions were used for the flow at the walls with zero flux for species transport. The overall external heat-transfer coefficient was set to zero to represent adiabatic conditions. Inlet boundary conditions for κ and ω were calculated via a prescribed turbulence intensity (5%) and specification of the inlet hydraulic diameter. The outlet was specified as a pressure outlet (0 Pa gauge pressure and zero gradients).

The 1D-SCM uses the same initial conditions as the 3D-CFD for the state inside the catalyst channel at $t = 0$ s. The inlet boundary conditions for the 1D-SCM are the same as those for the 3D-CFD. An in-house developed MATLAB code is used to obtain solutions to the 1D-SCM model (system of ODEs). In the comparison of results, the former are therefore time-shifted by $\Delta t = q_{in}/V_u$, where q_{in} is the volumetric flow rate (m³/s) and V_u is the volume upstream the catalyst brick in the 3D-CFD model (that is not present in the 1D-SCM).

RESULTS AND DISCUSSION

Validation of the Kinetics. In this section, we present a validation of our models against the findings reported by Pandya et al. (2009). This validation employed both 3D-CFD and 1D-SCM simulations to investigate the steady-state behavior at various temperatures (300 to 600 K). The catalyst geometry and operating conditions (gas hourly space velocity and inlet species concentrations) were maintained consistent with those reported by Pandya et al.[42] for all three cases.

Subsequent validation of both 3D-CFD and 1D-SCM simulation results was achieved against the experimental data from Pandya et al.[42] The kinetics model from Pandya et al.[42] was used, with reaction rates converted from kmol/² cat s to kmol/m³ s based on catalyst dimensions and specifications. The catalyst volume and reactor density were calculated, leading to the determination of the platinum mass, dispersion, and total surface area. The unknown catalyst surface-to-volume ratio served as a fitting parameter during this validation process and was verified by the nominal catalyst loading in terms of Wt % Pt. Figure 7 presents a detailed comparison between the results of our steady-state simulations and those of Pandya et al. (2009) for inlet temperatures ranging from 300 to 600 K (corresponding to case 1 in the terminology of Pandya et al.:[42] the concentrations of O_2, CO_2, and H_2O are 6%, 10%, and 10%, in the N_2 balance, as shown in Table 3). The comparison

Table 3. Operating Conditions Used for the Validation

GHSV (STP) (h⁻¹)	CO (ppm)	H₂ (ppm)	C₃H₆ (ppm)	NO (ppm)
50,000	100	33	350	150

reveals that the current simulations capture the light-off temperatures well, and the peak conversions and trends of the species CO and C_3H_6 agree with the experimental values. While a slight discrepancy is observed for the peak conversion of NO in our simulations, it is important to note that this behavior is also present in the simulations conducted by Pandya et al. (2009), this is possibly due to the multiple reactions involving NO. It is interesting to note that kinetic parameters were obtained by an optimization and model fitting procedure, and the model values of Pandya et al.[42] seem to overestimate the conversion of NO. It is important to note that our 3D-CFD has inlet diverging cones that present distribution of velocities and temperatures at the catalyst, whereas the 1D model of ours and that of Pandya et al.[42] do not have this distribution and radial heat transfer included in the model. The deviations of the simulation results from the experimental results can be attributed to these factors, as well.

Calibration Case and Test Cases. In this work, we choose to rely on a single calibration case to derive our MCM.
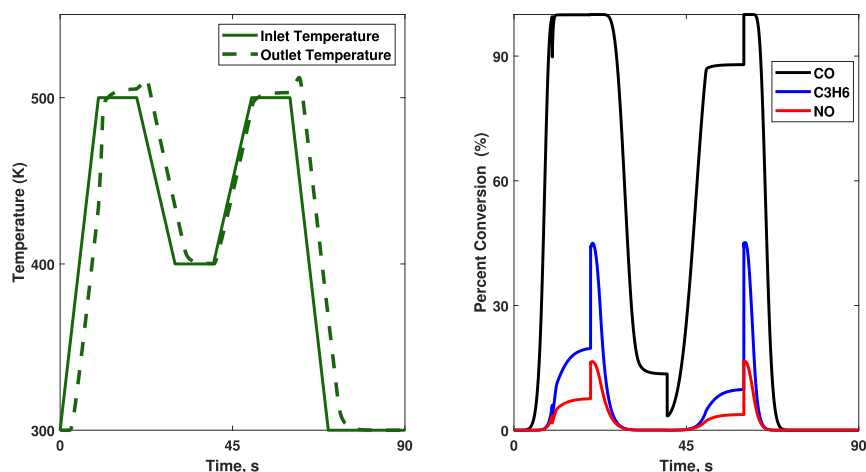
Figure 8. CFD results for the calibration case. The left panel shows the inlet and outlet temperatures as functions of time and the right panel shows the species conversions at the catalyst outlet plane as functions of time.

Thereafter, we apply the MCM to a series of test cases of increasing complexity, here characterized as being very different from the calibration case.

CFD Solution Analysis. Figure 8 shows the CFD results obtained for the calibration case. For this case, the inlet boundary conditions for mass flow rate, temperature, and species concentrations are depicted in Figure 3.

The outlet temperature resembles the inlet temperature with a time shift given by the retention time in the system and with a slight increase at the highest temperatures due to the contribution from the heats of reactions (all but NO_2 decomposition are exothermic reactions). The inlet temperature starts at low temperatures (cold start) and increases toward higher temperatures, passing light-off temperatures of first CO and thereafter C_3H_6 and NO. Complete conversion of CO happens relatively early, as the concentration of CO is low and CO lights off at temperatures around 473 K. The concentrations of C_3H_6 and NO at the inlet are higher, and the insufficient residence time at the temperatures seen renders peak conversions around 40% and 20%. NO conversion is also limited to reversible oxidation to NO_2.

Chemometric Analysis. *Data Preparation.* The CFD solution set is a matrix consisting of velocity, temperature, and nine species at the catalyst outlet plane, logged for the complete simulation duration of 90 s at a frequency of 10 ms. Our objective is to devise an MCM to predict the values of these solution variables at the outlet plane of the catalyst. The species N_2 is not considered in the analysis, as it is present in large excess and does not have a significant distribution or change in the simulation duration. The other eight species, namely, CO, O_2, C_3H_6, NO, NO_2, H_2, and H_2O are considered in the chemometric analysis. The outlet plane has 45 nodes along the radial direction. The matrix, therefore, has a size of 9000×450, as shown below

$$\begin{bmatrix} V_{(i_1,j_1)} \cdots V_{(i_1,j_n)} T_{(i_1,j_1)} \cdots T_{(i_1,j_n)} y_{1_{(i_1,j_1)}} \cdots y_{n_{(i_1,j_1)}} \cdots y_{n_{(i_1,j_n)}} \\ \cdots\cdots \\ V_{(i_n,j_1)} \cdots V_{(i_n,j_n)} T_{(i_n,j_1)} \cdots T_{(i_n,j_n)} y_{1_{(i_n,j_1)}} \cdots y_{n_{(i_n,j_1)}} \cdots y_{n_{(i_n,j_n)}} \end{bmatrix}$$

The subscripts i and j represent time and node locations, respectively, the first index is at 1 and the last at n. y_i represents the species mass fraction at the catalyst outlet plane. It is important to note that the number of rows and columns in the data set (on which PCA will be applied) represents the number of observations and variables, respectively. Our goal is to identify how many "channels" of the catalytic converter will be required to explain the variance of the data set. Therefore, the nodes will have to be in the "row" dimension. The CFD data set needs to be rearranged so that the nodes become observations. Velocity, temperature, and mass fraction of species at the nodes at time steps become variables. We collect the values of velocity at the 45 nodes at all time steps, resulting in a block of size of 45×9000, i.e., the first column represents the velocity at all nodes at time step 1. Similarly, the temperature and species mass fractions form the other blocks. These concatenated blocks each of size 45×9000 represent the variables for velocity, temperature, and species mass fractions, resulting in ten blocks (V, T, and eight species). Now, the resultant matrix will have size $45 \times 90,000$, i.e., 45 observations of 90,000 variables. The range of values of these variables varies significantly, so mean centering and unit-variance scaling are applied on the concatenated matrix prior to PCA. This normalization ensures that each variable contributes equally to the PCA analysis by centering the data set around the mean and scaling it by the variance. As a result, the origin of the concatenated data set is shifted to zero through mean centering, and normalizing by the variance ensures that every variable receives equal weightage in the PCA.

Principal Component Analysis. The noniterative partial-least-squares (NIPALS) algorithm is used to obtain the principal components.[50] An in-house code is solved in MATLAB (R2022b) to arrive at the number of principal components.

Additionally, due to temperature transients, species conversion fluctuates from 0% to 100% (particularly for CO). Depending on the value of the temperature in any plane in the catalyst, species concentration can all be equal, resulting in columns with zero variance. These columns are subsequently removed as those columns do not contribute to the model.

More than 99% of the variance is captured by the first five components (the eigenvalues after the first five components contribute minimally to the overall variance). Therefore, selecting these first five components allowed us to capture 99.21% of the total variance. This suggests that a MCM with five representative channels adequately characterizes the DOC.

Figure 9. Node locations chosen by D-optimal design. Nodes 1, 29, 35, 41, and 45 are chosen. Three of the five chosen nodes are located closer to the wall.

(Overall, the PCA was repeated for varying numbers of PCs in the range 1−20, and five were sufficient to capture most of the variance in the data set.) The optimum number of principal components chosen was evaluated based on multiple criteria such as setting threshold of cumulative variance, ratio of successive eigen values, and by identifying knee in the Scree plot of eigen values of the principal components.[51]

D-Optimal Design. The output plane of the catalyst is characterized by 45 node locations at which the solution variables are sampled. The first node designated by "Node 1" is on the axis (center), and the last node designated by "Node 45" is near the wall as shown in Figure 9. Our aim is to identify which among these nodes are effectively captured by the principal components. This is accomplished through D-optimal design applied to the scores matrix obtained from the PCA.

A candidate set was constructed utilizing the scores with five components. In our context, the size of the candidate set is 45 × 5, from which subsets will be selectively chosen. These chosen subsets serve as representations of the actual node locations within the outlet plane. To delineate the exact nodes, a model matrix X is formed from the candidate set, and the dispersion matrix is defined as $(X^T X)^{-1}$. Selecting a subset of the model matrix that minimizes the determinant of the dispersion matrix, as proposed by Smith,[44] yields the precise node locations. The MATLAB function candexch was employed with a specified maximum number of iterations to optimize node selection.[52] The D-optimal design results, as shown in Figure 9, indicate that the chosen set predominantly consists of outer channels. These channels exhibit substantial variability in velocity and temperature, induced by the tendency to flow recirculation at the periphery of the inlet cone.

Weighted Least-Squares. The effectiveness of the MCM is tested on the performance of the herein studied EATS by choosing two quantities, the heat content of the gas and the species conversion in the catalytic converter. These objective functions are a combination of the solution variables. The heat content of the gas is the product of mass flow rate, specific heat capacity, and temperature (relative to a reference temperature). The mass flow rate is itself a function of velocity, density (a function of temperature), and the cross-sectional area available for the flow. Species conversion is the ratio of the moles of a reactant reacted per mole of the reactant fed. We refer to the dependent variable or the response variable by Y, and $\overline{Y}$ is the mean of the response variable and X is the predictor or the independent variable.

Q_{tot} is the total heat carried by the gas. We can refer to the heat content as the outcome or response variable. The observed outcome of the heat content objective function is the sum of heat content of gas at all 45 nodes on the outlet plane. This is given by

$$Y = Q_{tot} = \Sigma_{k=1}^{45} q_k = \Sigma_{k=1}^{45} A_k u_k \rho_k C_p (T_k - T_{ref}) \tag{2}$$

The predicted outcome or response variable of heat content is the weighted average of the heat content of the channels picked up from the D-optimal design procedure for n_s channel locations and is given by

$$Q_s = \sum_{k=1}^{n_s=5} q_k = \sum_{k=1}^{n_s=5} w_k A_k u_k \rho_k C_p (T_k - T_{ref}) \tag{3}$$

If $Y = Q_{tot}$, $\overline{Y} = \text{mean}(Q_{tot})$ and $X = Q_s$, then the unknowns w_k are calculated by

$$w_k = (X^T X)^{-1} X^T (Y - \overline{Y}) \tag{4}$$

In the same way, we can define the conversion of species as the ratio of the moles of the species converted (reacted) to the moles of species present initially. This is given by

$$\chi_k = \frac{x_{A_0} - x_{A_{k,t}}}{x_{A_0}} \tag{5}$$

where x_{A0} and $x_{Ai,t}$ are the mole fractions of the species A present initially and at any time t in location k. The mean over all locations on the outlet plane gives the overall conversion. This is the objective function for the species conversion. We can then obtain the weights for this function by using WLS regression over this function.

Analysis of the Test Cases in Terms of Residuals and Root-Mean-Square of the Error. To quantify the accuracy attainable for the derived MCM, the heat content and species conversions are predicted for the channels from the D-optimal design with the weights from the WLS procedure. Thereafter, the residual, Ξ, is defined as the difference between the predicted value and the value from the CFD simulation

$$\Xi_Q = Q_{CFD} - Q_s \tag{6}$$

and

$$\Xi_{\chi_i} = \chi_{i_{CFD}} - \chi_{i_s} \tag{7}$$

The prediction error can be decreased by increasing the number of PCs and, hence, the number of channels. To enable a visualization of the results, a scaled prediction error E is defined as the ratio of residual in the variable Y at every time to the range of the variable in the residual. The choice of range scaling is made as the values of the predicted error preserve the trend in the unscaled data.

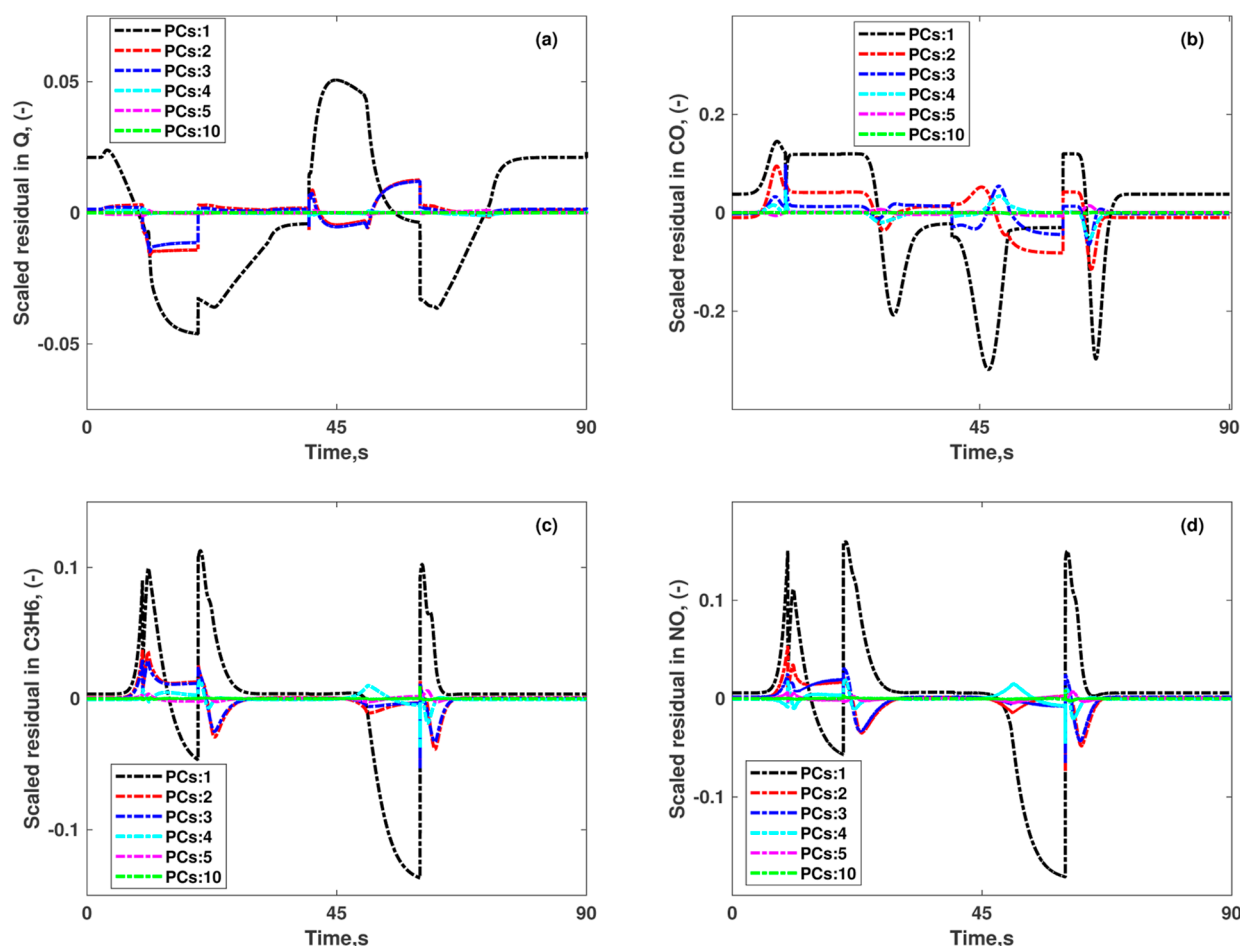$$E = \frac{\Xi_Y}{\max(Y) - \min(Y)} \tag{8}$$

Figure 10. Prediction errors E for varying number of retained PCs on the calibration set. Prediction error in (a) heat content, (b) CO conversion, (c) C_3H_6 conversion, and (d) NO conversion.

Figure 10 shows the plot of prediction errors in the heat content and species conversion over time for the calibration set. Here, the predicted solutions are from the same base solution set that was used in the PCA. The errors are plotted for a number of principal components. The prediction error is the largest when only a single PC is used for the prediction; however, this error is small even then. As the number of PCs increases beyond one, the prediction error decreases significantly. This analysis can be used as an alternative way to set a threshold value that can aid in choosing the number of PCs to be retained.

Figures 11 and 12 shows the prediction errors for test cases 2 and 3, respectively. (The methodology of analysis of prediction errors for test case 1 is similar to that of calibration set and the test cases 2 and 3, and similar results were obtained). In test case 2, the predicted set differed from the calibration set by a time-shifted velocity transient at the inlet. Due to this delay, the combination of residence times and temperature differs from the calibration case, affecting the reactions in terms of conversion and temperature of the gases. The MCM trained on the calibration data set has, therefore, not seen the exact combinations of inlet conditions met in this test case. Consequently, the prediction errors are slightly larger than those in the calibration set. Here again, the prediction error decreases with an increase in the number of PCs used. Figure 12 represents the analysis for test case 3, in which both velocity and species concentrations are different from those of

the calibration case. Unlike the constant species concentration used in the calibration case, test case 3 features time-varying species concentrations. Despite these significant differences in the inlet profile compared to the calibration case, the prediction errors remain comparable.

Figure 13 compares the root-mean-square error (RMSE) of all of the predictions. RMSE is the average of the squared magnitude of residuals (deviations of the predicted values from the true 3D-CFD solution), and it is therefore a metric to compare prediction accuracy. In this comparison, five PCs were retained for developing the MCM. The errors for heat content are in the order of a few watts and the predicted conversion has an error of less than 1% for all cases. The largest RMSE for the MCM is seen for test case 3, which has a different transient inlet velocity and species concentrations than the calibration set. The error is significantly larger for the SCM, showcasing the superior reliability of the MCM to the conventional approach, even in extrapolation scenarios.

Figure 14 shows the predicted catalyst performance for the MCM developed by retaining five PCs and contrasts the performance of the MCM against the conventional SCM and the full CFD. The MCM agrees very well with the full CFD solution, in particular peak conversions and transients are well captured. The SCM shows larger discrepancies to the full CFD solution in terms of accurately predicting peak conversions.

In the case of flow maldistribution, which is practically unavoidable in a realistic EATS due to space limitations
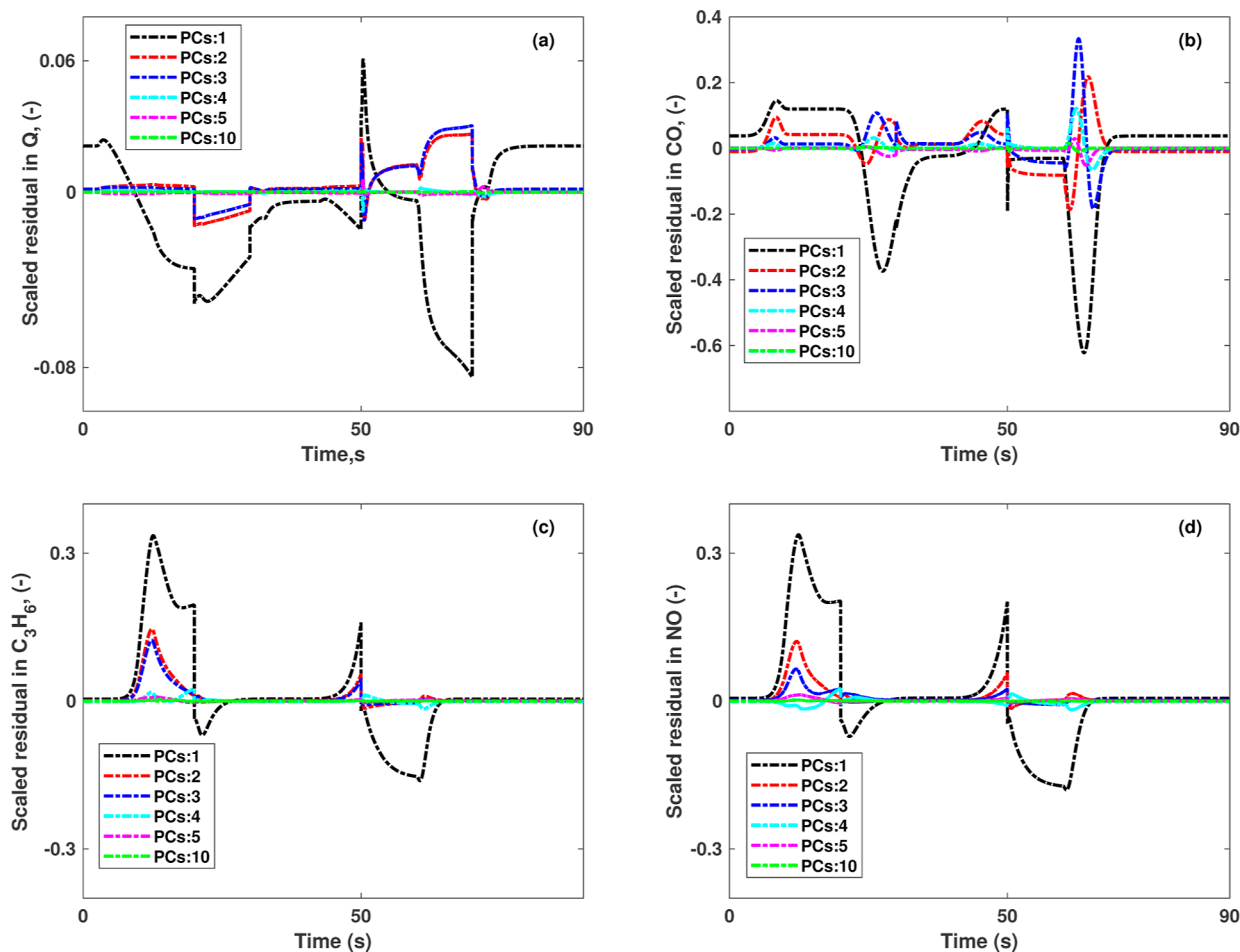
Figure 11. Prediction errors E for varying number of retained PCs on the test case 2. This test case differs from the calibration set by the velocity transient, by a time shift of 10 s. Prediction error in (a) heat content, (b) CO conversion, (c) C_3H_6 conversion, and (d) NO conversion.

(forcing designs with sharp bends and cone diffusers), velocity, temperature, and species concentration exhibit significant spatiotemporal variations. In a 3D-CFD model, these variations are intrinsically resolved, and the catalyst performance can be predicted while accounting for the aforementioned effects. In an SCM, on the other hand, the spatial distribution is averaged to a single value. As catalyst conversion is highly nonlinear, this averaging has severe adverse effects on the accuracy and reliability of the predicted conversion. The MCM proposed here is developed by capturing the variance of the base CFD solution, and the predictions are much better than the equivalent SCM.

COMPUTATIONAL EFFICIENCY

The simulations were carried out on a computer installed with i7 processor (at 3.19 GHz) and 64 GB RAM and Table 4 gives the computational costs comparison. The 3D-CFD simulations employed fixed time stepping and took 17−27 h per case including file I/O operations. The 1D-SCM simulations used adaptive time stepping and required 2.5−19.2 min per case. For both methods, the cases with varying inlet concentrations were more costly due to stiffness.

The corresponding MCM simulations were completed in less than 2 min for the three steps, viz., PCA, D-optimal design, and the WLS. This required the data set from the CFD simulations to be available for processing for PCA. Even so, the largest computational cost of the MCM is associated with the

data collection from the CFD. Thus, with the availability of data from CFD simulations, MCM requires up to 1 order of magnitude less computational time than the SCM. Furthermore, the MCM, once constructed, is significantly faster than real-time (more than 1 order of magnitude) and thus the only method of the three applicable for onboard diagnostics and control.

CONCLUSIONS

In the present work, a methodology for the development of a MCM for catalytic converters is demonstrated by applying MVDA (PCA and D-optimal design) and WLS regression on a state-of-the-art transient 3D-CFD reactive simulations output. The method combines CFD data with chemometric techniques to accomplish model order reduction. A DOC with diverging cones was chosen as the base model to demonstrate and evaluate the performance of the MCM. The monolith catalyst was represented by a porous media approximation. Transient mass flow rate, temperature, and species concentrations were applied at the inlet, and the solution variables were collected at the catalyst outlet.

These inlet profiles were used to develop and test the MCM and were termed the calibration case and the test cases. Scaling and pretreatment of the calibration data set were done before the PCA. Five components were sufficient to explain 99.21% of the variance of the data set. The D-optimal design procedure on the scores of the chosen principal components produced
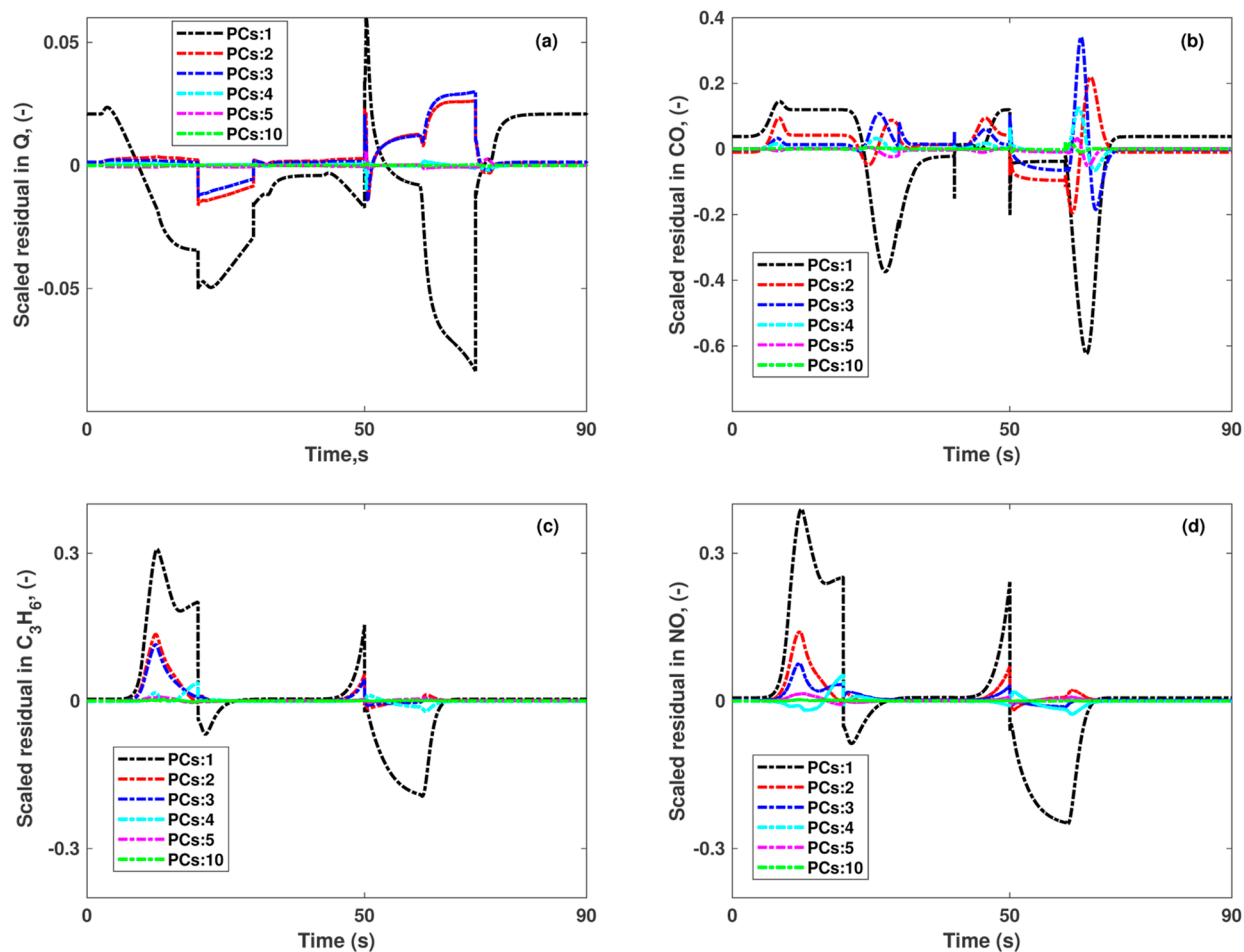
Figure 12. Prediction errors E for varying number of retained PCs on the test case 3. This test case differs from the calibration set by a time shift of 10 s in the velocity transient and a variable concentration profile for the species CO and H_2. Prediction error in (a) heat content, (b) CO conversion, (c) C_3H_6 conversion, and (d) NO conversion.
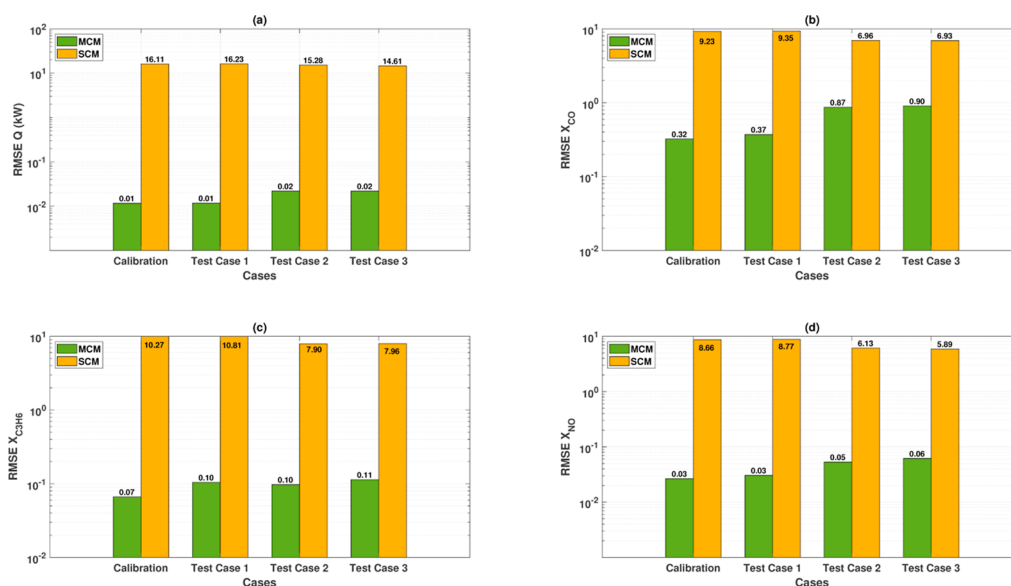

Figure 13. Performance comparison of the developed MCM and the 1D-SCM against the 3D-CFD for heat content and species conversion. Panels (a–d) are the RMSE comparisons for the heat content and conversions of the species CO, C_3H_6, and NO, respectively. Logarithmic axis is used as the SCM RMSE is much larger in magnitude than the RMSE of the MCM.
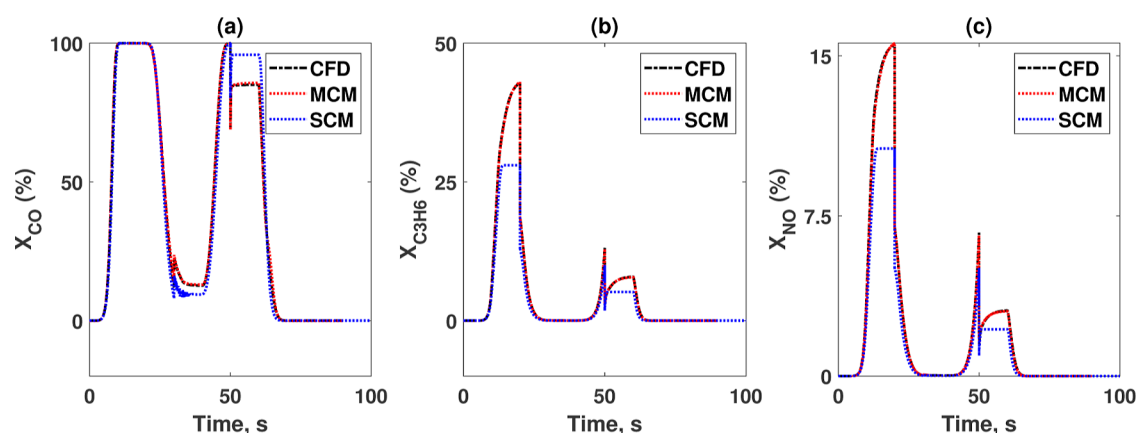
Figure 14. Predicted values of species conversion plotted against time. Panels (a−c) show the percentage conversions for CO, C_3H_6, and NO, respectively. Five PCs were retained to obtain the MCM predictions. These predictions are compared to the results from both CFD and 1D-SCM simulations. The MCM predictions are in an excellent agreement with the CFD results, indicating that the MCM accurately captures the conversion behavior for these species.

Table 4. Computational Costs Associated with the Different Modelling Strategies/Steps of the Current Work

case	CFD (h)	MCM				SCM (min)
		data collection (s)	PCA (s)	D-optimal design (s)	WLS (s)	
calibration case	17.2	83	5.2	2.1	1.9	2.5
test case 1	26.3				4.3	19.2
test case 2	17.0				4.5	4.4
test case 3	26.8				4.1	16.8
total	87	105				43

the channel locations in the outlet plane. Of the five channels picked by the D-optimal design, three were closer to the wall, one each at the center and interior, respectively.

These channels were then combined by a WLS procedure, by choosing the total heat content of the gas and conversion of the species as objective functions. The output of the full CFD model was compared with the MCM and a SCM for the two objective functions. The residuals of the MCM were small, and the results were overall very similar to those of the CFD. The SCM had larger residuals than the MCM, proving the attainable accuracy of the MCM. Performances were compared in terms of the root-mean-square of the error in the objective functions. The performances of the MCM with all the test cases compared closer to the CFD results than the SCM, which cannot adequately capture spatiotemporal variations in inlet conditions arising from flow maldistribution.

This work represents the first application of combining CFD analysis with chemometric techniques to develop a reduced-order model for an EATS application. This work is intended as a proof-of-concept that can be applied to other EATS-components, such as SCR reactors. The computational effort required to create the MCM is comparable to that of SCM, provided that the base CFD data is available. Alternatively, experimental measurements can also be used as a calibration set. These models can be used rigorously for control applications with improved accuracy and fidelity at low computational cost completely unattainable for conventional SCMs or full-scale CFD. The methodology developed here has no limitations in terms of geometric complexity and can therefore easily be extended to real-life EATS with bends, cones, diffusers, and parallel reactors. It is recommended that this work be extended by comprehensive testing of the proposed procedure using a realistic driving cycle and investigate the effectiveness of smaller calibration data sets, despite the significant computational demands.

■ ASSOCIATED CONTENT

Ⓢ Supporting Information

The Supporting Information is available free of charge at https://pubs.acs.org/doi/10.1021/acs.iecr.4c01571.

> Multivariate data analysis, governing equations for the 3D-CFD model, and model equations for a single channel model (PDF)

■ AUTHOR INFORMATION

Corresponding Authors

Henrik Ström − *Division of Fluid Dynamics, Department of Applied Mechanics and Maritime Sciences, Chalmers University of Technology, Gothenburg 41296, Sweden;* ⓞ orcid.org/0000-0002-8581-5174; Email: henrik.strom@chalmers.se

Jonas Sjöblom − *Division of Energy Conversion and Propulsion Systems, Department of Applied Mechanics and Maritime Sciences, Chalmers University of Technology, Gothenburg 41296, Sweden;* Email: jonas.sjoblom@chalmers.se

Author

Pratheeba Chanda Nagarajan − *Division of Energy Conversion and Propulsion Systems, Department of Applied Mechanics and Maritime Sciences, Chalmers University of Technology, Gothenburg 41296, Sweden;* ⓞ orcid.org/0000-0002-0738-5041

Complete contact information is available at:
https://pubs.acs.org/10.1021/acs.iecr.4c01571

Notes

The authors declare no competing financial interest.

■ ACKNOWLEDGMENTS

■ REFERENCES

(1) Manisalidis, I.; Stavropoulou, E.; Stavropoulos, A.; Bezirtzoglou, E. Environmental and health impacts of air pollution: a review. *Public Health Front.* **2020**, *8*, 14.

(2) Emissions in the automotive sector. https://ec.europa.eu/growth/sectors/automotive-industry/environmental-protection/emissions-automotive-sector_en (accessed Sept, 2024).

(3) Heck, R. M.; Farrauto, R. J.; Gulati, S. T. *Catalytic Air Pollution Control: Commercial Technology*; John Wiley & Sons, 2016.

(4) Hettel, M.; Wörner, M.; Deutschmann, O. *Handbook of Materials Modeling: Applications: Current and Emerging Materials*; Springer, 2020; Chapter: Computational Fluid Dynamics of Catalytic Reactors, pp 1405−1438.

(5) Ström, H.; Sasic, S. Heat and mass transfer in automotive catalysts—The influence of turbulent velocity fluctuations. *Chem. Eng. Sci.* **2012**, *83*, 128−137.

(6) Walander, M.; Sjöblom, J.; Creaser, D.; Agri, B.; Löfgren, N.; Tamm, S.; Edvardsson, J. Modelling of mass transfer resistances in non-uniformly washcoated monolith reactors. *Emiss. Control Sci. Technol.* **2021**, *7*, 153−162.

(7) Hayes, R. E. *Introduction to Catalytic Combustion*; Routledge, 2021.

(8) Ozhan, C.; Fuster, D.; Da Costa, P. Multi-scale flow simulation of automotive catalytic converters. *Chem. Eng. Sci.* **2014**, *116*, 161−171.

(9) Young, L. C.; Finlayson, B. A. Mathematical models of the monolith catalytic converter: Part I. Development of model and application of orthogonal collocation. *AIChE J.* **1976**, *22*, 331−343.

(10) Young, L. C.; Finlayson, B. A. Mathematical models of the monolith catalytic converter: Part II. Application to automobile exhaust. *AIChE J.* **1976**, *22*, 343−353.

(11) Oh, S. H.; Cavendish, J. C. Transients of monolithic catalytic converters. Response to step changes in feedstream temperature as related to controlling automobile emissions. *Ind. Eng. Chem. Prod. Res. Dev.* **1982**, *21*, 29−37.

(12) Hoebink, J.; Van Gemert, R.; Van Den Tillaart, J.; Marin, G. Competing reactions in three-way catalytic converters: modelling of the NOx conversion maximum in the light-off curves under net oxidising conditions. *Chem. Eng. Sci.* **2000**, *55*, 1573−1581.

(13) Holder, R.; Bollig, M.; Anderson, D.; Hochmuth, J. A discussion on transport phenomena and three-way kinetics of monolithic converters. *Chem. Eng. Sci.* **2006**, *61*, 8010−8027.

(14) Hayes, R.; Mukadi, L.; Votsmeier, M.; Gieshoff, J. Three-way catalytic converter modelling with detailed kinetics and washcoat diffusion. *Top. Catal.* **2004**, *30/31*, 411−415.

(15) Mladenov, N.; Koop, J.; Tischer, S.; Deutschmann, O. Modeling of transport and chemistry in channel flows of automotive catalytic converters. *Chem. Eng. Sci.* **2010**, *65*, 812−826.

(16) Hayes, R.; Liu, B.; Votsmeier, M. Calculating effectiveness factors in non-uniform washcoat shapes. *Chem. Eng. Sci.* **2005**, *60*, 2037−2050.

(17) Joshi, S. Y.; Harold, M. P.; Balakotaiah, V. On the use of internal mass transfer coefficients in modeling of diffusion and reaction in catalytic monoliths. *Chem. Eng. Sci.* **2009**, *64*, 4976−4991.

(18) Papadias, D.; Edsberg, L.; Björnbom, P. Simplified method for effectiveness factor calculations in irregular geometries of washcoats. *Chem. Eng. Sci.* **2000**, *55*, 1447−1459.

(19) Lundberg, B.; Sjöblom, J.; Johansson, Å.; Westerberg, B.; Creaser, D. DOC modeling combining kinetics and mass transfer using inert washcoat layers. *Appl. Catal., B* **2016**, *191*, 116−129.

(20) Walander, M.; Sjöblom, J.; Creaser, D.; Lundberg, B.; Tamm, S.; Edvardsson, J. Efficient experimental approach to evaluate mass transfer limitations for monolithic DOCs. *Top. Catal.* **2019**, *62*, 391−396.

(21) Kočí, P.; Marek, M.; Kubíček, M.; Maunula, T.; Härkönen, M. Modelling of catalytic monolith converters with low-and high-temperature NO_x storage compounds and differentiated washcoat. *Chem. Eng. J.* **2004**, *97*, 131−139.

(22) Katare, S. R.; Patterson, J. E.; Laing, P. M. Diesel Aftertreatment Modeling: A Systems Approach to NOx Control. *Ind. Eng. Chem. Res.* **2007**, *46*, 2445−2454.

(23) Hettel, M.; Daymo, E.; Schmidt, T.; Deutschmann, O. CFD-Modeling of fluid domains with embedded monoliths with emphasis on automotive converters. *Chem. Eng. Process.* **2020**, *147*, 107728.

(24) Mei, H.; Li, C.; LiU, H.; Ji, S. Simulation of Catalytic Combustion of Methane in a Monolith Honeycomb Reactor. *Chin. J. Chem. Eng.* **2006**, *14*, 56−64.

(25) Kumar, A.; Mazumder, S. Toward simulation of full-scale monolithic catalytic converters with complex heterogeneous chemistry. *Comput. Chem. Eng.* **2010**, *34*, 135−145.

(26) Koltsakis, G.; Konstantinidis, P.; Stamatelos, A. Development and application range of mathematical models for 3-way catalytic converters. *Appl. Catal., B* **1997**, *12*, 161−191.

(27) Windmann, J.; Braun, J.; Zacke, P.; Tischer, S.; Deutschmann, O.; Warnatz, J. Impact of the inlet flow distribution on the light-off behavior of a 3-way catalytic converter. *SAE Technical Paper Series*; SAE International 2003; pp 713−723.

(28) Agrawal, G.; Kaisare, N. S.; Pushpavanam, S.; Ramanathan, K. Modeling the effect of flow mal-distribution on the performance of a catalytic converter. *Chem. Eng. Sci.* **2012**, *71*, 310−320.

(29) Karvounis, E.; Assanis, D. N. The effect of inlet flow distribution on catalytic conversion efficiency. *Int. J. Heat Mass Transfer* **1993**, *36*, 1495−1504.

(30) Hayes, R. E.; Fadic, A.; Mmbaga, J.; Najafi, A. CFD modelling of the automotive catalytic converter. *Catal. Today* **2012**, *188*, 94−105.

(31) Liu, Z.; Benjamin, S. F.; Roberts, C. A. Pulsating flow maldistribution within an axisymmetric catalytic converter-flow rig experiment and transient cfd simulation. *SAE Technical Paper Series*; SAE International 2003, 2003-01-3070.

(32) Chanda Nagarajan, P.; Ström, H.; Sjöblom, J. Numerical Assessment of Flow Pulsation Effects on Reactant Conversion in Automotive Monolithic Reactors. *Catalysts* **2022**, *12*, 613.

(33) Dammalapati, S.; Aghalayam, P.; Kaisare, N. Modeling the Effects of the Inlet Manifold Design on the Performance of a Diesel Oxidation Catalytic Converter. *Ind. Eng. Chem. Res.* **2021**, *60*, 3860−3870.

(34) Chanda Nagarajan, P.; Ström, H.; Sjöblom, J. Transient Flow Uniformity Evolution in Realistic Exhaust Gas Aftertreatment Systems Using 3D-CFD. *Emiss. Control Sci. Technol.* **2022**, *8*, 154−170.

(35) Chakravarthy, V.; Conklin, J.; Daw, C.; D'Azevedo, E. Multi-dimensional simulations of cold-start transients in a catalytic converter under steady inflow conditions. *Appl. Catal., A* **2003**, *241*, 289−306.

(36) Weltens, H.; Bressler, H.; Terres, F.; Neumaier, H.; Rammoser, D. Optimisation of catalytic converter gas flow distribution by CFD prediction. *SAE Technical Paper Series*; SAE International, 1993; p 930780.

(37) Canu, P.; Vecchi, S. CFD simulation of reactive flows: Catalytic combustion in a monolith. *AIChE J.* **2002**, *48*, 2921−2935.

(38) Aslanjan, J.; Klauer, C.; Perlman, C.; Günther, V.; Mauß, F. Simulation of a three-way catalyst using a transient multi-channel model. *SAE Technical Paper Series*; SAE International, 2017, 2017-01-0966.

(39) Della Torre, A.; Montenegro, G.; Onorati, A.; Cerri, T.; Tronconi, E.; Nova, I. Numerical optimization of a SCR system based on the injection of pure gaseous ammonia for the NO reduction in light-duty diesel engines. *SAE Technical Paper Series*; SAE International, 2020, 2020-01-0356.

(40) Sutherland, J. C.; Parente, A. Combustion modeling using principal component analysis. *Proc. Combust. Inst.* **2009**, *32*, 1563−1570.

(41) Aversano, G.; Bellemans, A.; Li, Z.; Coussement, A.; Gicquel, O.; Parente, A. Application of reduced-order models based on PCA & Kriging for the development of digital twins of reacting flow applications. *Comput. Chem. Eng.* **2019**, *121*, 422−441.

(42) Pandya, A.; Mmbaga, J.; Hayes, R.; Hauptmann, W.; Votsmeier, M. Global kinetic model and parameter optimization for a diesel oxidation catalyst. *Top. Catal.* **2009**, *52*, 1929−1933.

(43) Greenacre, M.; Groenen, P. J.; Hastie, T.; d'Enza, A. I.; Markos, A.; Tuzhilina, E. Principal component analysis. *Nat. Rev. Methods Primers* **2022**, *2*, 100.

(44) Smith, K. On the standard deviations of adjusted and interpolated values of an observed polynomial function and its constants and the guidance they give towards a proper choice of the distribution of observations. *Biometrika* **1918**, *12*, 1−85.

(45) Minkowycz, W.; Haji-Sheikh, A.; Vafai, K. On departure from local thermal equilibrium in porous media due to a rapidly changing heat source: the Sparrow number. *Int. J. Heat Mass Transfer* **1999**, *42*, 3373−3385.

(46) Santos, H.; Costa, M. The relative importance of external and internal transport phenomena in three way catalysts. *Int. J. Heat Mass Transfer* **2008**, *51*, 1409−1422.

(47) Kyle, B. G. *Chemical and Process Thermodynamics*; Prentice-Hall, Inc.: Englewood Cliffs, NJ, 1984.

(48) Kee, R. J.; Coltrin, M. E.; Glarborg, P. *Chemically Reacting Flow: Theory and Practice*; John Wiley & Sons, 2005.

(49) Fogler, H. *Elements of Chemical Reaction*; Pearson Education, 2020.

(50) The NIPALS Algorithm. https://cran.r-project.org/web/packages/nipals/vignettes/nipals_algorithm.html (accessed Sept, 2024).

(51) Sclove, S. L. *Advances in Principal Component Analysis*; InTech Open, 2022; Chapter: Determining an Adequate Number of Principal Components, pp 139−154.

(52) candexch. https://se.mathworks.com/help/stats/candexch.html (accessed Sept, 2024).